Acta Mechanica Sinica (2019) 35(4):713–728
https://doi.org/10.1007/s10409-019-00874-x

RESEARCH PAPER

Boundary layer structure in turbulent Rayleigh–Bénard convection in a slim box

Hong-Yue Zou[1] · Wen-Feng Zhou[1] · Xi Chen[1] · Yun Bao[2] · Jun Chen[1] · Zhen-Su She[1]

Received: 25 August 2018 / Revised: 28 November 2018 / Accepted: 17 January 2019 / Published online: 5 June 2019

Abstract
Logarithmic boundary layers have been observed in different regions in turbulent Rayleigh–Bénard convection (RBC). However, how thermal plumes correlate with the logarithmic law of temperature and how the velocity profile changes with pressure gradient are not fully understood. Here, we perform three-dimensional (3D) simulations of turbulent Rayleigh–Bénard convection in a slim box without the front and back walls, with aspect ratio width:depth:height $= L{:}D{:}H = 1{:}1/6{:}1$ (corresponding to the x, y, and z coordinates, respectively), in the Rayleigh number $Ra = [1 \times 10^8, 1 \times 10^{10}]$ for Prandtl number $Pr = 0.7$. To investigate the structures of the viscous and thermal boundary layers, we examine the velocity profiles in the streamwise and vertical directions (i.e. U and W) along with the mean temperature profile throughout the plume-impacting, plume-ejecting, and wind-shearing regions. The velocity profile is successfully quantified by a two-layer function of a stress length,, $\ell_u^+ = \ell_0^+ (z^+)^{3/2} \left[1 + \left(z^+/z_{\rm sub}^+\right)^4\right]^{1/4}$, as proposed by She et al. (J Fluid Mech, 2017), though it is neither Prandtl–Blasius–Pohlhausen (PBP) type nor logarithmic. In contrast, the temperature profile in the plume-ejecting region is logarithmic for all simulated cases, attributed to the emission of thermal plumes. The coefficient of the temperature log law, A, can be described by the composition of the thermal stress length $\ell_{\theta 0}^*$ and the thicknesses of thermal boundary layer $z_{\rm sub}^*$ and $z_{\rm buf}^*$, i.e. $A \simeq z_{\rm sub}^* / \left(\ell_{\theta 0}^* {z_{\rm buf}^*}^{3/2}\right)$. The adverse pressure gradient responsible for turning the wind direction contributes to intensively emitting plumes and the logarithmic temperature profile at the plume-ejecting region. The Nusselt number scaling and the local heat flux in the slim box are consistent with previous results for confined cells. Therefore, the slim-box RBC is a preferred system for investigating in-box kinetic and thermal structures of turbulent convection with the large-scale circulation in a fixed plane.

Keywords Rayleigh–Bénard convection · Wall-bounded turbulence · Heat transport · Direct numerical simulation

1 Introduction

Rayleigh–Bénard convection (RBC) is commonly used to study natural convection, due to the simplicity of its configuration and the richness of its flow regimes. In this system, fluid is filled in a closed cell, heated on the bottom and cooled on the top, with adiabatic side no-slip wall [1–3]. The control parameters are the Rayleigh number $Ra = g\beta\Delta T H^3/(\nu\kappa)$, the Prandtl number, $Pr = \nu/\kappa$, and the aspect ratio $\Gamma = L/H$, where ν is the kinematic viscosity, κ is the thermal diffusivity, H is the height of the sample, L is its width, g is the gravitational acceleration, β is the thermal expansion coefficient, and ΔT is the temperature difference between the top and bottom plate. Enhancement of the heat transport of a natural convection system such as the RBC is particularly useful in many industrial processes and is of fundamental interest [4,5].

The boundary layer (BL) in RBC exhibits a transition from a laminar to a turbulent regime when Ra exceeds a critical value, Ra_c. In the laminar regime, the mean velocity profile (MVP) takes a Prandtl–Blasius–Pohlhausen (PBP) type,

Electronic supplementary material The online version of this article (https://doi.org/10.1007/s10409-019-00874-x) contains supplementary material, which is available to authorized users.

✉ Jun Chen
jun@pku.edu.cn

[1] State Key Laboratory for Turbulence and Complex Systems, Department of Mechanics and Engineering Science, College of Engineering, Peking University, Beijing 100871, China

[2] Department of Mechanics, College of Engineering, Sun Yat-sen University, Guangzhou 510275, China

whereas in the turbulent regime, a logarithmic (log) profile is usually expected, when an analogy is made with a BL passing a flat plate. A BL equation for RBC of $Pr > 1$ was recently developed [6] considering both laminar and turbulent contributions, and a model describing the mean profiles of temperature and its variance in the near-wall region was experimentally tested [7]. For $Ra < Ra_c$, the RBC-BL presents a PBP-like profile when measured at near-wall regions in zero pressure gradient (ZPG) conditions [8,9]. Nevertheless, the lateral change in the profile is remarkable, presenting significant deviations from the PBP-type at high Ra number [10,11].

The logarithmic mean temperature profile (MTP) is another issue which has recently garnered much attention in numerical and experimental studies, for Ra ranging from 10^{10} to 10^{15} [12–14]. Logarithmic temperature profiles were observed near the sidewalls in experiments and direct numerical simulations (DNS), which showed markedly decreased thickness near the middle of the conducting plate. The mechanism behind the log law of the MTP is still debated—whether it is induced by the momentum transport near the no-slip sidewall, by the heat transport due to emitted plumes, or by both, is still unknown. Some results indicate a correlation between the intensive plume emission and the logarithmic temperature profile. In a cylindrical container at $\Gamma \simeq 1$, the plumes are found to be abundantly emitted from the top/bottom plate near the sidewalls, leading to an intensive local heat flux [15]. In a recent two-dimensional (2D) DNS study with a horizontal periodic boundary, a vertical log MTP only appears in the regions where plumes accumulate [16]. However, the physics in these regions is still not fully understood.

Most previous experimental and numerical studies of the RBC system set the horizontal section in a circular or square geometry, where the large-scale circulation (LSC) exhibits frequent reversal, cessation or azimuthal motion [17,18]. In such systems, the plume-emitting regions appear to 'wander' along the conducting plate, and it is difficult to extract the property of a certain flow region free of the influence from other regions. Similar phenomena have been observed in the cubic box ($L{:}D{:}H = 1{:}1{:}1$), where the large-scale convection is found to exhibit random reorientation of the LSC and low-frequency oscillation perpendicular to the LSC [19]. Complex convection flow also appears in a rectangular container for $Ra = 8 \times 10^8 \sim 1 \times 10^{10}$, due to strong secondary flow in the form of horizontal rolls surrounding the core of the cell and orthogonal to the cross-stream rolls [20]. Thus, neither a cubic cell nor a rectangular cavity is appropriate to establish a turbulent RBC with a statistically steady LSC over a large range of Ra.

We perform a three-dimensional (3D) simulation with an LSC in a fixed plane so that a statistical mean field can be studied in great detail. This is achieved by reducing the scale in the depth direction to make a slim box, e.g. $L{:}D{:}H = 1{:}1/6{:}1$, for which the mean flow becomes ideally confined in the vertical plane. It has been reported that the aspect ratio in the planes perpendicular to the LSC, D/L, has strong effects on the global heat transport—the increased wall friction and suppressed LSC lead to more coherent and energetic plumes emitted from the conducting plates and thus enhancement of the global heat transport [21]. The focus of the present study is to investigate a steady LSC in a plane free from the wall/confinement effect. This helps to settle down a better defined statistical mean field with well-defined flow regions. The periodic condition in the depth (y) direction allows for velocity and temperature fluctuating over a range of scales smaller than $1/6$ of the depth of the box. Meanwhile, it is wide enough to develop relevant turbulent thermal convection for the simulated Ra. This configuration will be referred to as the slim-box RBC simulation, in which a turbulent LSC is confined in a fixed plane. Compared to other RBC systems of $D/L \simeq 1$, the slim-box simulation establishes a stronger and more stable LSC with an unchanged wind direction. It will be seen that the periodic boundary condition in the y direction somewhat mimics the rectangular cell; indeed, the measured velocity and temperature profiles averaged in the depth direction present relevant features of experimental and numerical results previously observed.

We focus on the characteristics of the convection flow in different regions. An outcome of the current simulation, in addition to the LSC and the corner roll [22], is the identification of three flow regions, namely plume-impacting, wind-shearing and plume-ejecting regions, in a time-averaged velocity field, similar to the results for 3D DNS of the RBC in a circular cylinder [23]. Note that the RBC in the slim box has a larger LSC, a result of the absence of friction due to sidewalls. The coherent motion of the stronger LSC yields a thinner viscous BL and hence a larger Reynolds number. The Nusselt number Nu in the present study is also slightly larger than that in a confined cell, as measured at the same Pr [24].

The mean horizontal and vertical velocity (U and W) and temperature profiles in the slim box (averaged in the depth direction) are measured and studied in great detail in three regions, i.e. plume-ejecting, wind-shearing, and plume-impacting, for the medium Rayleigh number. Because of the strong adverse pressure gradient in the wind-shearing and plume-ejecting regions, the BL in RBC is very different from a turbulent BL on a flat plate, so that neither a PBP-type nor the log-law BL is indeed observed in the MVP. On the other hand, the multilayer theory proposed by She et al. [25] allows us to analytically quantify the kinetic BL by means of a two-layer stress-length function.

For the MTP, the plume-ejecting region is found to hold a logarithmic region in all simulated cases, in agreement with previous studies. This logarithmic layer, however, is one of the multilayer structures for the temperature length, and the log-law coefficient, A, can be related to the thick-

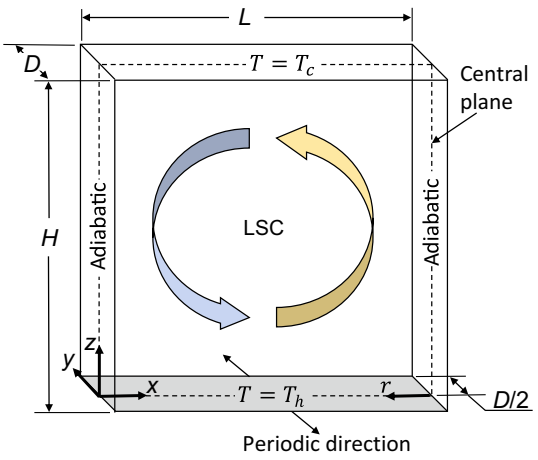

Fig. 1 Sketch of the convection box showing the definitions of coordinates and dimensions. The plane marked by a dashed line is the location of the side view of the convection

ness of the sublayer and buffer layer, which are measured at all streamwise locations and shown to exhibit a two-layer structure away from the ejection corner of the RBC cell. This model, for the first time, yields a two-dimensional (2D) temperature mean field, in agreement with DNS data, which is superior to the result obtained by Grossmann et al. [26] (i.e. $|A| = |A_1|/\sqrt{4x(1-x)}$). The relation between the log law of MTP and the emission of thermal plumes, previously suggested by a two-dimensional simulation of RBC [16], is confirmed in our 3D simulations, and the role of the adverse pressure gradient is emphasized.

The paper is organized as follows. In Sect. 2, we discuss the numerical simulation method. Section 3 contains the results and discussion, including temperature and pressure distribution, the mean velocity and temperature profiles, and the heat flux distribution in the slim box. Concluding remarks are given in Sect. 4.

2 Numerical setup

The choice of the geometrical configuration is based on the following considerations. When the scale in the depth direction is reduced to form a slim box (with e.g. $L{:}D{:}H = 1{:}1/6{:}1$, where L, D, H denote horizontal x, depth y and vertical z directions, respectively, and with a vertical aspect ratio $\Gamma = L/H = 1$), the mean flow is confined in the vertical plane (at least approximately). Figure 1 schematically displays the geometry of the slim box and the LSC. The periodic boundary condition set in the y direction allows for velocity and temperature fluctuation over a range of scales smaller than 1/6 of the length of the box.

We numerically integrate the incompressible Navier-Stokes equation with the Boussinesq approximation and the continuity equation, following Ref. [27]:

$$\frac{\partial \boldsymbol{u}}{\partial t} + (\boldsymbol{u}\cdot\nabla)\boldsymbol{u} = -\nabla p + \theta \boldsymbol{e}_z + \nu\nabla^2\boldsymbol{u}, \tag{1}$$

$$\frac{\partial \theta}{\partial t} + (\boldsymbol{u}\cdot\nabla)\theta = \kappa\nabla^2\theta, \tag{2}$$

$$\nabla\cdot\boldsymbol{u} = 0, \tag{3}$$

where $\boldsymbol{e}_z$ is the unity vector pointing in the opposite direction to gravity, $\boldsymbol{u}$ is the velocity vector, p is the reference pressure and θ is the nondimensional temperature (with $\pm 1/2$ at the bottom and top walls). The integrated equations are normalized using the free-fall velocity $U = \sqrt{RaPr}(\kappa/H)$, the reference pressure $P_0 = RaPr(\rho\kappa^2)/H^2$, and the time scale $T_0 = (H^2/\kappa)\sqrt{RaPr}$.

The fluid in the slim-box RBC is bounded in the $x-z$ plane by the upper and lower isothermal plates and adiabatic sidewalls, so the boundary conditions are $\partial\theta/\partial x|_{x=0} = \partial\theta/\partial x|_{x=L} = 0$. No-slip and impenetrability conditions are used for all solid boundaries. Periodicity is assumed in the y direction, i.e. $\theta|_{y=0} = \theta|_{y=D}$, $\partial\theta/\partial y|_{y=0} = \partial\theta/\partial y|_{y=D}$, $\boldsymbol{u}|_{y=0} = \boldsymbol{u}|_{y=D}$, and $\partial\boldsymbol{u}/\partial y|_{y=0} = \partial\boldsymbol{u}/\partial y|_{y=D}$).

All the simulations were performed with a second-order finite-difference code, see Ref. [28] for details. Due to the absence of singularity at the origin, the central second-order finite difference was applied in the y direction. A time-splitting method extensively discussed in Refs. [29, 30] was used for the time advancement. The third-order low-storage Runge–Kutta method, along with the Crank–Nicolson scheme, was implemented to evaluate the non-solenoidal velocity [30]. The finite-difference scheme for the temperature equation is the same as that for velocity, except for pressure-related terms.

Solving the Poisson equation for pressure requires that the solution be sufficiently smooth up to the boundary. The iterative method is inefficient at high Ra when small-scale fluctuations are abundantly developed. We thus applied the fast fourier transformation (FFT) method to alter the parallel diagonal dominant (PDD) solver from 3D to 2D, see Ref. [31] for details.

Keeping the grid spacing smaller than the Kolmogorov scale η_K and the Batchelor scale η_B over the whole domain is important to ensure proper spatial resolution [32], where $\eta_K = (\nu^3/\epsilon_u)^{1/4} = Pr^{1/2}Ra^{-1/4}(Nu-1)^{-1/4}H$, and $\eta_B = \eta_K/\sqrt{Pr}$ [33]. The time step was chosen to satisfy the Courant–Friedrichs–Lewy (CFL) condition, i.e. CFL $\leqslant 0.2$. In our simulations, Nu was calculated by integrating over the whole volume and over time. Table 1 reports the minimum and maximum grid spacings, $\Delta_{\min}$ and $\Delta_{\max}$, which are indeed smaller than η_B and η_K; thus, the finest scales in the bulk flow are well resolved. The thermal BL thickness was then calculated using the relation of $\lambda_\theta = H/(2Nu)$. The Bolgiano length scale was evaluated using $L_B = \langle\epsilon_u\rangle^{5/4}/(g^2\beta^2\langle\epsilon_\theta\rangle)^{3/4} \approx Nu^{1/2}Pr^{-1/4}Ra^{-1/4}H$, where ϵ_θ is the thermal dissipation rate [32].

Table 1 Numbers of the grids $N_x \times N_y \times N_z$, values of the Nusselt number estimated by three different methods Nu_1, Nu_2, Nu_3, the minimum and maximum slim-box sizes $\Delta_{\min}$ and $\Delta_{\max}$, the Bolgiano length scale L_B, the Kolmogorov viscous scale η_K, and the Batchelor scale η_B

Ra	$N_x \times N_y \times N_z$	Nu_1	Nu_2	Nu_3	$\Delta_{\min}$	$\Delta_{\max}$	L_B	η_K	η_B
1×10^8	$768 \times 128 \times 512$	34.7	34.2	34.3	0.23×10^{-3}	4.2×10^{-3}	6.44×10^{-2}	3.47×10^{-3}	4.15×10^{-3}
5×10^8	$768 \times 128 \times 512$	55.8	54.8	55.3	0.45×10^{-3}	1.4×10^{-3}	5.42×10^{-2}	2.00×10^{-3}	2.41×10^{-3}
1×10^9	$768 \times 256 \times 800$	68.9	69.3	68.5	0.08×10^{-3}	1.6×10^{-3}	5.10×10^{-2}	1.64×10^{-3}	1.96×10^{-3}
5×10^9	$1024 \times 256 \times 800$	110.8	109.1	109.7	0.20×10^{-3}	1.8×10^{-3}	4.31×10^{-2}	0.97×10^{-3}	1.20×10^{-3}
1×10^{10}	$1600 \times 512 \times 1600$	144.6	147.4	143.2	0.05×10^{-3}	0.8×10^{-3}	4.16×10^{-2}	7.60×10^{-4}	9.08×10^{-4}

An additional control for DNS quality is to compare different Nu using different integration procedures. One way is to compute the heat flux directly by integrating along the two conducting walls, i.e. $Nu_1 = -\partial\Theta/\partial z$ at the upper ($z = H$) or the lower ($z = 0$) plates. The second is to compute the volume-averaged temperature dissipation ε_θ or energy dissipation ε_u [34], yielding $Nu_2 = \langle\varepsilon_\theta\rangle$ or $Nu_3 = 1 + Pr\langle\varepsilon_u\rangle$, respectively, where $\langle\cdot\rangle$ denotes the ensemble average over both time and space. As reported in Table 1, these Nusselt numbers are in good agreement with each other, ensuring the statistical convergence of the simulated RB system.

A well-resolved simulation at high Ra requires a large computation resource. The simulations employed up to 1024 TH-1A CPUs (central processing units), using $768 \times 128 \times 512$ grids for $Ra = 1 \times 10^8$ and 1×10^9, and $1600 \times 512 \times 1600$ grids for $Ra = 1 \times 10^{10}$. In order to examine the turbulent state of the RBC flow, we placed 8 probes at different heights, from $z/H = 9.8 \times 10^{-3}$ to $z/H = 0.25$ at the centerline, i.e. $x/L = 0.5$ and $y/D = 0.5$. These probes record point-wise fluctuating temperature $\theta(t)$ and velocity (of three components $u(t)$, $v(t)$, and $w(t)$). Figure 2 shows that the flow is in a developing stage before $t = 30$, and then reaches a statistically steady state after $t = 40$. The positive correlation between fluctuating velocity, $u(t)$, and fluctuating temperature, $\theta(t)$, is seen for the fluid near the bottom plate, as seen in Fig. 2c, d, respectively.

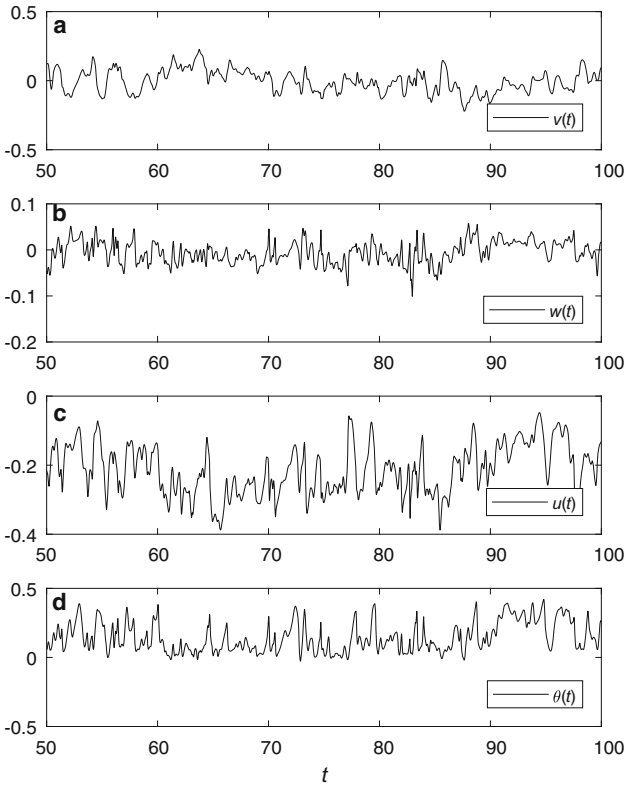

Fig. 2 Signals of a numerical probe located halfway down the slim box at $z/H = 9.8 \times 10^{-3}$, $x/L = 0.5$, and $y/D = 0.5$, for $Ra = 1 \times 10^8$

3 Results and discussion

3.1 Temperature and pressure distributions

Figure 3 presents snapshots of the temperature and pressure isosurface for $Ra = 1 \times 10^8$, showing that the LSC is confined in the $x-z$ plane. It can also be seen that three-dimensionality is remarkable in the near-wall region, where thermal plumes are intensively emitted. However, temperature and pressure within the LSC remain almost unchanged in the y direction, indicating that the LSC is characterized by quasi-two-dimensional flow.

The data are collected for comparison with experimental and other DNS studies including the viscous BL thickness and heat flux. This consists of two sets of experimental measurements [35,36], two sets of DNS from Ref. [37] with different aspect ratios and from Stevens et al. [38] for a cylindrical box with aspect ratio $\Gamma = 1/2$ at higher Ra of 2×10^{10}, 2×10^{11} and 2×10^{12}. Mean streamwise velocity measurements from du Puits et al. [39] at several Ras around 1×10^{11} and mean temperature measurements from Ref. [13] are also compared with the present simulations. For convenience, we summarize these DNS and experimental results in Table 2.

Ensemble average is carried out by integrating in the depth (y) direction and in time. The mean velocity, temperature and pressure distribution at $Ra = 1 \times 10^8$ and 1×10^9 are shown in Fig. 4. The mean flow is represented by a counterclockwise rotation at the center of the box. As Ra increases, the high-

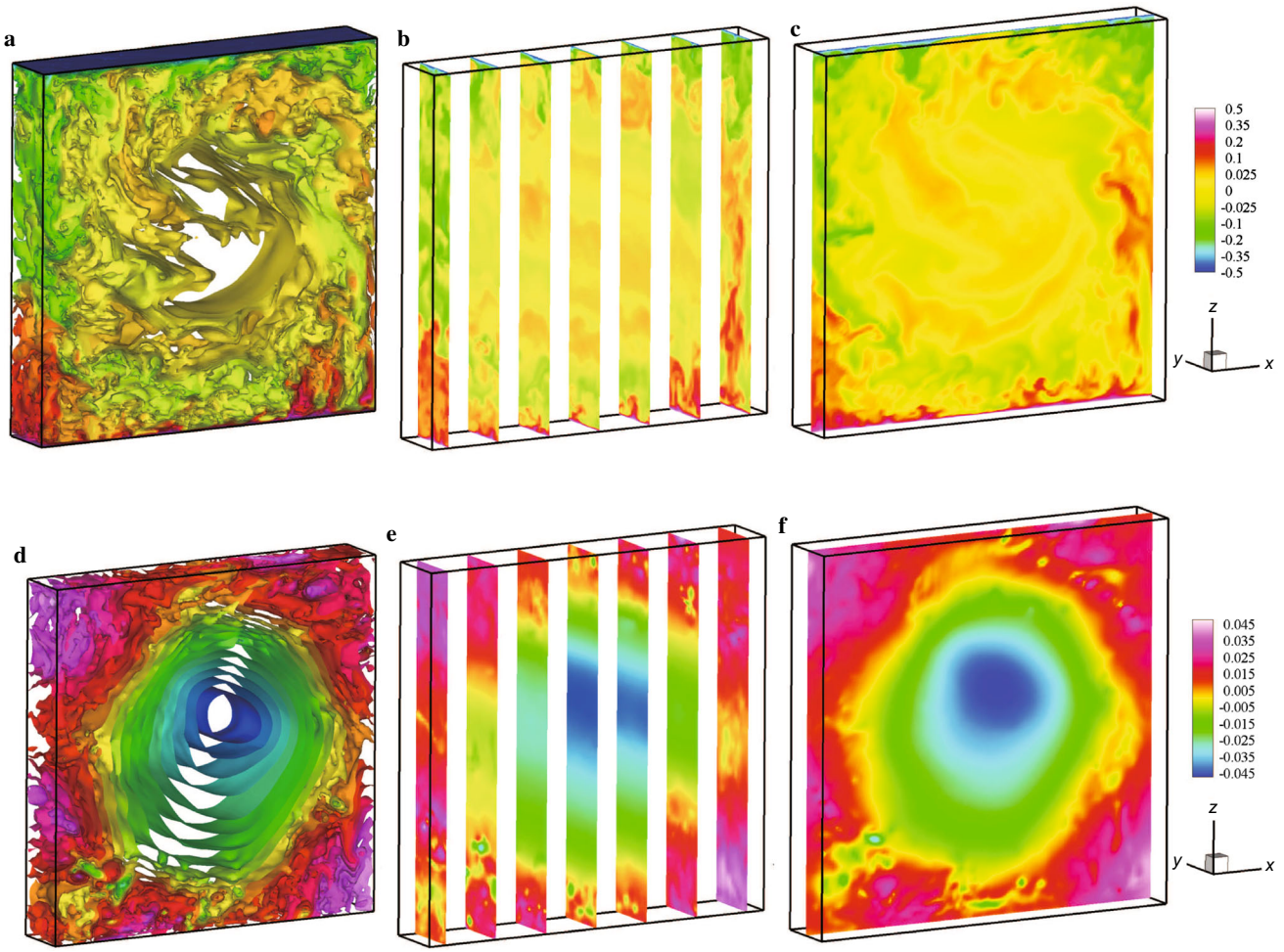

Fig. 3 Visualization of the instantaneous **a, b, c** temperature and **d, e, f** pressure. The color in plots **a**–**c** denotes temperature, and the color in plots **d**–**f** denotes pressure. The slices in plots **b** and **e** are the corresponding fields in the $y-z$ planes at various streamwise (x) locations. The fields shown in plots **c** and **f** are the fields in the $x-z$ plane on the halfway point of the depth of the box. These snapshots are obtained from the simulation at $Ra = 1 \times 10^8$ and $Pr = 0.7$

Table 2 Parameters of DNS and experiments

Case	References	Ra	Pr	$L{:}D{:}H$ (rectangular) or $L{:}H$ (cylindrical)	Confinement shape	Data
DNS-A	Present study	$1 \times 10^8 \sim 1 \times 10^{10}$	0.7	1:1/6:1	Rectangular	$U, W, \theta, Nu, \lambda_u$
DNS-B	[38]	$2 \times 10^{10} \sim 2 \times 10^{12}$	0.7	1:2	Cylindrical	Nu, θ
DNS-C	[37]	$1 \times 10^7 \sim 1 \times 10^{10}$	0.7, 4.38	1:1/64:1 $\sim$ 1:1:1	Rectangular	Nu
EXP-A	[39]	$1.2 \times 10^{11} \sim 9.8 \times 10^{11}$	0.7	1:1.13	Cylindrical	U
EXP-B	[13]	$4 \times 10^{12} \sim 1 \times 10^{15}$	0.8	1:2	Cylindrical	θ
EXP-C	[35]	$1 \times 10^9 \sim 1 \times 10^{10}$	4.3	25:7:24	Rectangular	Re, λ_u, U
EXP-D	[36]	$2.4 \times 10^8 \sim 5.6 \times 10^9$	5.3	1:1	Cylinder	Re, λ_u

speed fluid shifts towards the border of the box, along with a slower-rotating LSC. A pair of corner rolls, as the secondary flow induced by the LSC, exist in the respective corners on the diagonal line of the box. They have been reported in previous experimental [40–42] and numerical studies [11,43,44]. An analytic model for the corner rolls in turbulent RBC was recently reported by Zhou and Chen [22].

Figure 4 shows that the positive high pressure coincides with the regions of intensively ejecting plumes, corresponding to the lower right and upper left corners of the slim box. The center of the box, on the other hand, corresponds to a low-pressure zone, as shown in Fig. 4b, d. This indicates that the pressure gradient maintains a balance with the centrifugal force. Similarly, the cores of two corner rolls are closely asso-

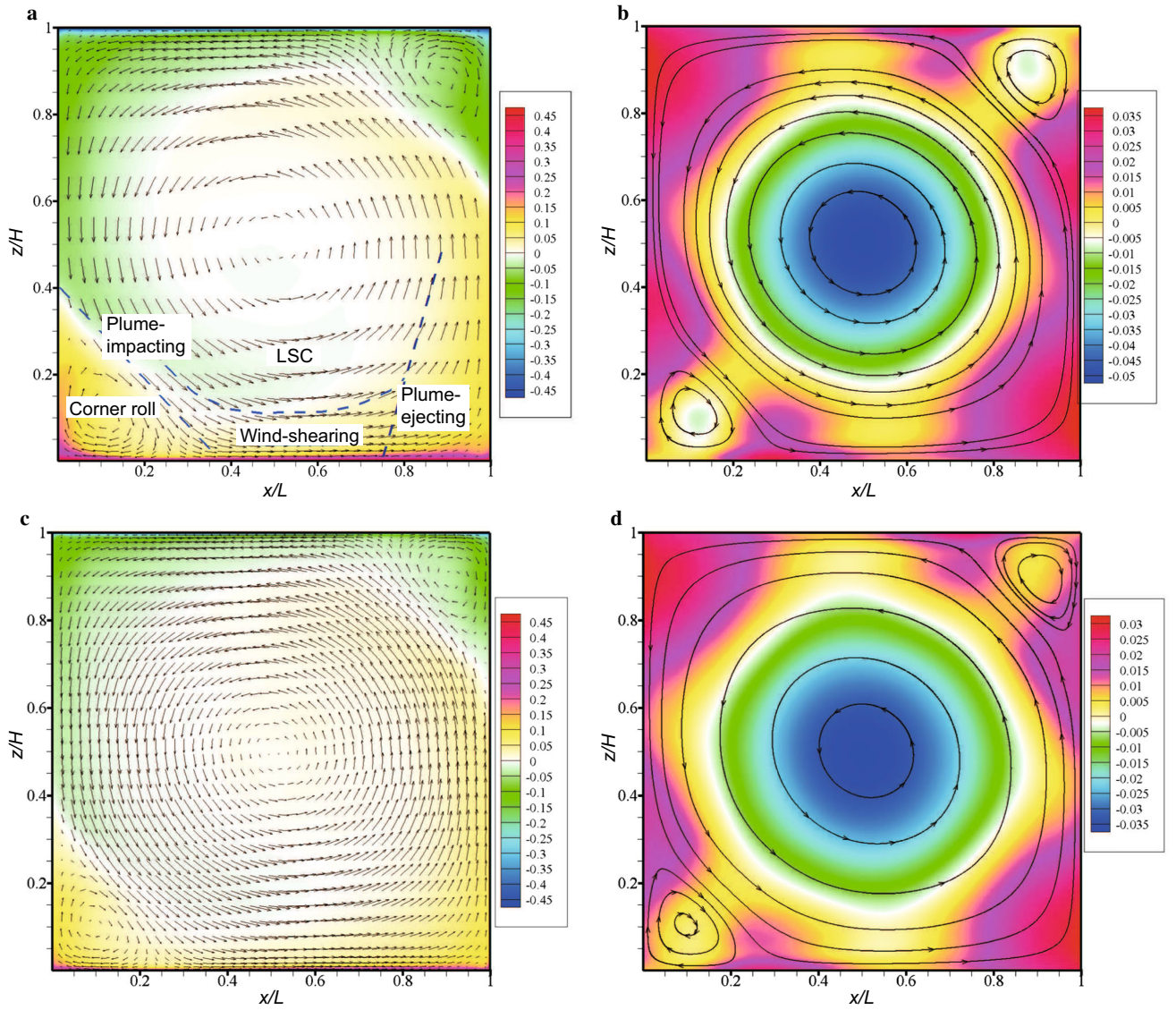

Fig. 4 Time-averaged 2D distribution of pressure and temperature displayed by pseudo-colors at $Ra = 1 \times 10^8$ in plots **a**, **b** and $Ra = 1 \times 10^9$ in plots **c**, **d**, respectively. The arrows indicate the velocity vectors. The rotatory LSC, the corner roll, and the plume-impacting, wind-shearing and plume-ejecting regions are marked by dashed lines in plot **a**. The lines with arrows in plots **b** and **d** are the time-averaged streamlines

ciated with two lower-pressure zones, which were observed in 2D simulations [45]. Note that the 3D corner roll is a smaller than the 2D one at $Ra = 1 \times 10^8$. Furthermore, the 3D simulation presents a more round-shaped LSC and a perceptibly wider wind-shearing region than the 2D simulation, indicating that the three-dimensionality of the near-wall corner flow is remarkable. This result is consistent with the previous numerical study [22].

Based on the averaged flow in the $x-z$ plane, we characterize the RBC flow by five regions: (1) the LSC motion in bulk, (2) the corner roll, (3) the plume-impacting regions above the corner rolls with ($0 \leqslant x \leqslant 0.25$), (4) the wind-shearing regions towards the middle of the conducting plates ($0.25 \leqslant x \leqslant 0.75$), and (5) the plume-ejecting region ($0.75 \leqslant x \leqslant 1$). The last three regions clearly possess a turbulent BL at a large aspect ratio, cf. Ref. [16]. Note that the change in flow direction at the corners signifies the presence of a high-pressure gradient [46,47], as consistently presented in Fig. 4b, d.

According to the correlation between the pressure and velocity fields, one can see that in the wind-shearing region, the BL flow is driven by the longitudinal pressure gradient. The fluid near the bottom plate is advected from a favorable pressure gradient region to an adverse pressure gradient

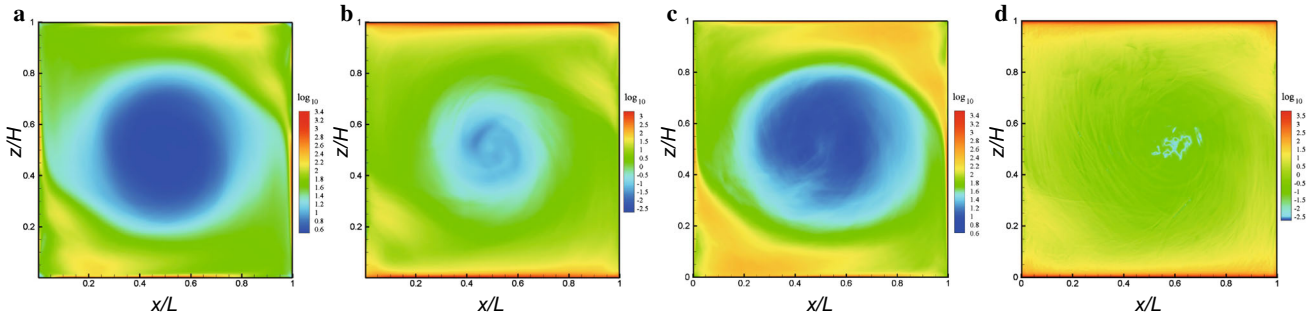

Fig. 5 **a, c** Spatial average along the y-axis of momentum dissipation ε_u and **b, d** thermal dissipation ε_θ for $Ra = 1 \times 10^8$ in plots **a**, **b** and for $Ra = 1 \times 10^9$ in plots **c**, **d**, respectively

(APG) region. The APG in relation to the flow direction is present in the plume-ejecting region, and is responsible for the change in the flow direction from horizontal to vertical. This makes RBC-BL distinct from canonical BL under ZPG conditions. Consequently, the viscous BL of turbulent RBC is not always of the PBP-type. In Sect. 3.2, we will discuss the structure of the viscous BL by analyzing the MVP in detail.

Figure 5a, c shows the distribution of momentum dissipation ε_u for $Ra = 1 \times 10^8$ and $Ra = 1 \times 10^9$, respectively, and the thermal dissipation ε_θ is shown in Fig. 5b, d. Note that the maximum of both ε_u and ε_θ are extremely close to the bottom/top plates. On the other hand, the variation in ε_θ near the sidewalls is moderate, due to the adiabatic wall condition, while ε_u exhibits a significant enhancement in the plume-impacting region (i.e. left-down and right-up corner of Fig. 5a, c). In contrast, both ε_θ and ε_u are low in the bulk zone, corresponding to the core of the LSC.

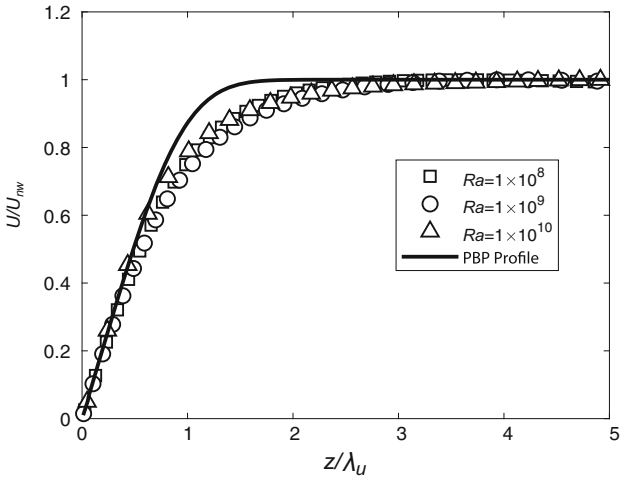

Fig. 6 MVPs at the box center ($Ra = 1 \times 10^8 \sim 1 \times 10^{10}$), with the PBP profile (solid line). Note that z is normalized by the thickness of the viscous BL, λ_u, defined by the near-wall maximum velocity

3.2 Multilayer structure of velocity profiles

The vertical MVPs at the center of the wind-shearing region ($x/L = 0.5$) against the PBP-type profiles for different Ras are shown in Fig. 6. It is clearly seen that the MVPs differ markedly from the PBP-type profile, especially near the conducting plates. The deviation from the PBP-type profile has also been reported in the literature (cf. Refs. [36,39]).

The mean horizontal velocity $U(z)$ at $x/L = 0.5$, and the mean vertical velocity $W(x)$ at $z/H = 0.5$ are shown in Fig. 7. A linear profile is found at the core of the LSC for both $U(z)$ and $W(x)$, indicating a solid rotation of fluid in this region (for $0.25 \leqslant z/H \leqslant 0.75$ in Fig. 7a and $0.25 \leqslant x/L \leqslant 0.75$ in Fig. 7b). Linearity of MVPs has been experimentally observed in both rectangular [48] and cylindrical cells [49]. The slim-box simulations show that the linear core of the LSC extends to the scale of $0.4L$ for all Ras, quite similar to that observed in a narrow 3D RBC cell with $D/H \simeq 1/4$ [48] and that in a cylindrical cell [49]. We also note that the humps of velocities appear at the border of the LSC for the U and W profiles, which determine the characteristic LSC velocities, $U_{\rm lc}$ and $W_{\rm lc}$, respectively. They are distinct from peak velocities near the wall, as denoted by $U_{\rm nw}$ and $W_{\rm nw}$, respectively.

Compared with the confined cell [48], the slim box with periodic boundary condition has a higher $U_{\rm lc}$ and a relatively large linear core. On the other hand, the $W_{\rm lc}$ is on the order of $W_{\rm nw}$, see Fig. 7. In particular, for the horizontal velocity at $x/L = 0.5$, $U_{\rm lc}$ is greater than $U_{\rm nw}$ for all Ras, indicating that near-wall buoyancy is overwhelmed by the wind shearing. With increasing Ra, both $U_{\rm lc}$ (and $W_{\rm lc}$) and $U_{\rm nw}$ (and $W_{\rm nw}$) tend to decrease, but the linear core velocity is more sharply decreased than that near the wall.

The thickness of the viscous BL as a critical quantity for turbulent BL is calculated. Several definitions of BL thickness have been suggested [35]. Here we use the thickness of BL, λ_u, obtained by extrapolation of the linear profile $U(z)$ to reach $U_{\rm nw}$. Note that λ_u is a dimensionless parameter normalized by the height of the box, H. Figure 8a shows that λ_u is smaller than the values measured in two experiments in

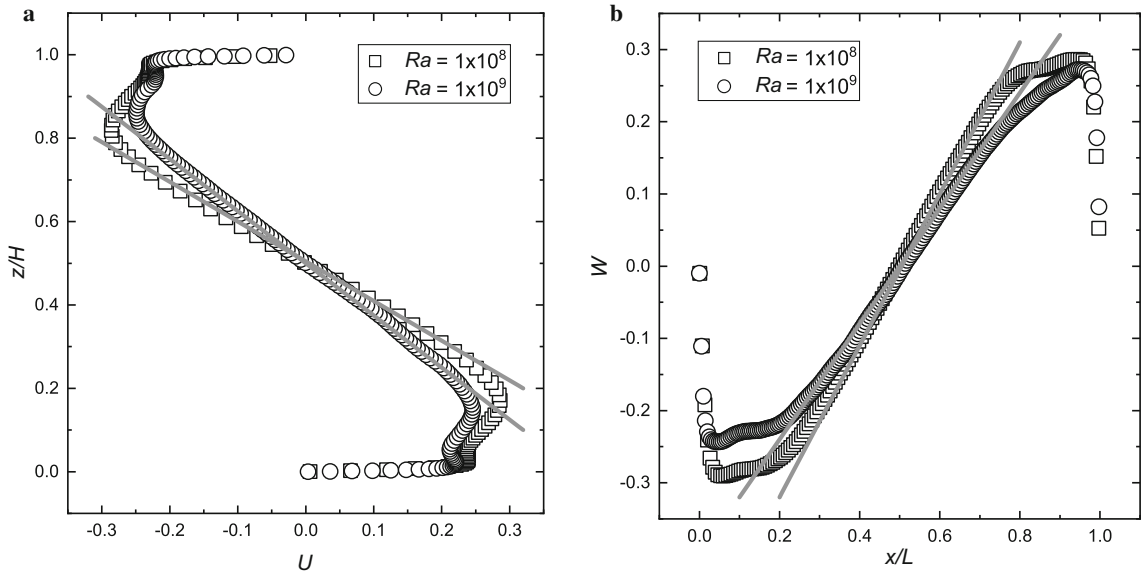

Fig. 7 **a** Horizontal velocity profile $U(z)$ cut along the z axis (at $x = 0.5$). **b** Vertical velocity profile $W(x)$ cut along the x axis (at $z = 0.5$)

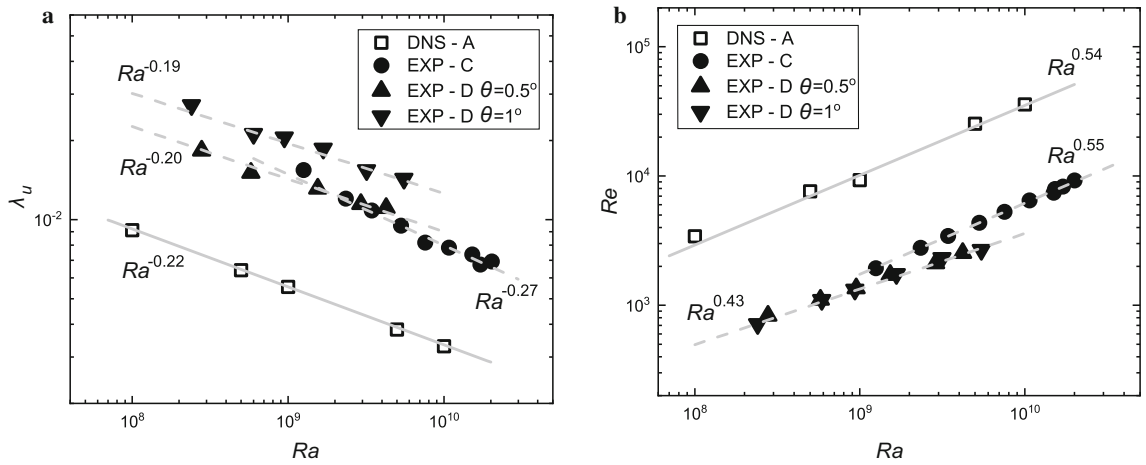

Fig. 8 Effects of the Rayleigh number on the thickness of the viscous BL and the Reynolds number. **a** Ra-dependence of the viscous boundary thickness normalized by H. **b** Ra-dependence of Re

confined cells [35,36]. A confined LSC tends to establish a steadier circulation in the cell. The experimental study with a tilted cylindrical cell showed that a larger tilt angle imposes a stronger restriction on the azimuthal motion of the LSC so that it has less fluctuation perpendicular to the wind [36]. The experiments with a slender rectangular cell also indicated that the confinement of the LSC tends to stabilize the large-scale flow structure and to establish a thinner viscous BL [35], as also shown in Fig. 8a. In the present study, the slim box almost eliminates the azimuthal meandering of the LSC. The relatively small value of λ_u for the slim-box flow is attributed to the absence of the depth confinement, and thus the wall friction, which allows us to develop a stronger LSC (with larger U_{nw}) at a larger scale, leading to a thinner viscous BL in comparison with the confined cell. The present simulations give a scaling of $\lambda_u \sim Ra^{-0.22}$, similar to the scaling of -0.20 in Ref. [36], but different from -0.27 in Ref. [35].

The mean velocity of the LSC reaches a maximum U_{nw}, relevant for determining the thickness of the viscous BL. Here, we present the bulk Reynolds numbers defined by $Re = U_{\mathrm{nw}}H/\nu$ against Ra obtained from the simulations and two other experiments in Fig. 8b. Because of the large U_{nw} in the present simulations, the Res of the simulations are always larger than the experimental measurements. Again, the present results show a scaling ($Re \propto Ra^{0.54}$), close to that of [35] ($Re \propto Ra^{0.55}$), in contrast to a smaller slope $Re \propto Ra^{0.43}$ [36].

The BL thickness over the entire wind-shearing region is calculated (i.e. $0.3 < x < 0.8$) to illustrate the streamwise

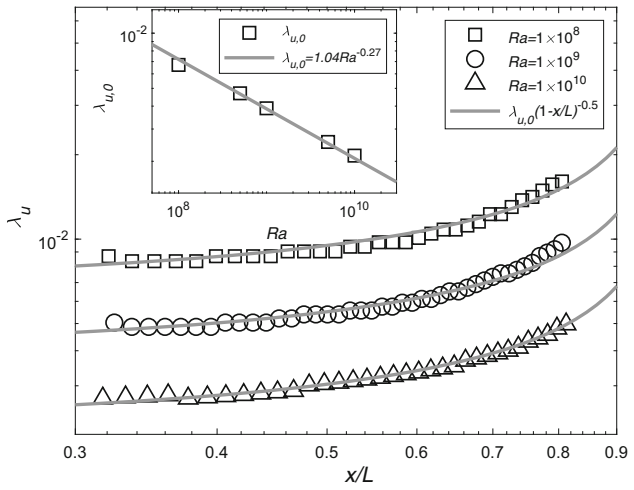

Fig. 9 Thickness of the viscous BL as a function $\lambda_u = \lambda_{u,0}(1 - x/L)^{-0.5}$, represented by solid lines

change in the viscous BL. Figure 9 shows $\lambda_u(x)$ at three Ras. A monotonic increase in the thickness can be described in a power law, $\lambda_u = \lambda_{u,0}(1 - x/L)^{-0.5} \propto r^{-0.5}$, where $r = 1 - x/L$ is the distance to the ejection corner of the cell. The inset of Fig. 9 shows the variation in the coefficient $\lambda_{u,0}$ as a function of Ra, presenting a scaling law of $\lambda_{u,0} = 1.04Ra^{-0.27}$. Thus, the BL thickness is expressed in the form of a power function, $\lambda_u(x) = 1.04Ra^{-0.27}r^{-0.5}$, in the wind-shearing region for all simulations.

To quantify MVP in the wind-shearing region, we follow the SED theory [25] to employ the stress length as the similarity variable, which takes a multilayer formula describing the structure in the direction normal to the wall. Neglecting the relatively small variation along the direction parallel to the wall in the mean momentum equation (i.e. the incompressible BL approximation), one obtains the following balance equations:

$$\nu\frac{\partial^2\overline{u}}{\partial z^2} - \frac{\partial\overline{u'w'}}{\partial z} = 0, \tag{4}$$

$$\nu\frac{\partial^2\overline{w}}{\partial x^2} - \frac{\partial\overline{w'u'}}{\partial x} = 0. \tag{5}$$

Equation (4) holds for $\overline{u}$ in the wind-shearing region (near $x/L = 0.5$), and Eq. (5) for $\overline{w}$ near $z/H = 0.5$. Integrating Eq. (4) along z and Eq. (5) along x yields

$$\frac{\partial\overline{u}^+}{\partial z^+} - \overline{u'w'}^+ = 1, \tag{6}$$

$$\frac{\partial\overline{w}^+}{\partial x^+} - \overline{w'u'}^+ = 1. \tag{7}$$

Note that $u^+ = u/u_\tau$, $z^+ = z/\delta_u$ and $\overline{u'w'}^+ = \overline{u'w'}/u_\tau^2$, where $u_\tau = \sqrt{\nu\partial u/\partial z|_{z=0}}$ and $\delta_u = \nu/u_\tau$. Similarly, we have $w^+ = w/w_\tau$, $x^+ = x/\delta_w$ and $\overline{w'u'}^+ = \overline{w'u'}/w_\tau^2$, where $w_\tau = \sqrt{\nu\partial w/\partial x|_{x=0}}$ and $\delta_w = \nu/w_\tau$. Introducing $S_u^+ = \frac{\partial\overline{u}^+}{\partial z^+}$ ($S_w^+ = \frac{\partial\overline{w}^+}{\partial x^+}$) and $W_u^+ = -\overline{u'w'}^+$ ($W_w^+ = -\overline{w'u'}^+$) gives a normalized mean velocity equation as

$$S_{\rm u}^+(z^+) + W_u^+(z^+) = 1, \tag{8}$$

$$S_{\rm w}^+(x^+) + W_w^+(x^+) = 1. \tag{9}$$

We emphasize that Eqs. (8) and (9) hold when the relatively small pressure gradient effect in the wind-shearing region is neglected. Introducing the stress length $\ell_{\rm u}^+ = \sqrt{W_u^+/S_{\rm u}^+}$ (and $\ell_{\rm w}^+ = \sqrt{W_w^+/S_{\rm w}^+}$), we have the solutions of Eqs. (8) and (9):

$$\frac{\partial\overline{u}^+}{\partial z^+} \approx \frac{2}{1+\sqrt{1+4\ell_{\rm u}^{+2}}}, \tag{10}$$

$$\frac{\partial\overline{w}^+}{\partial x^+} \approx \frac{2}{1+\sqrt{1+4\ell_{\rm w}^{+2}}}. \tag{11}$$

The theory developed by She et al. [25] allows us to construct the two-layer similarity solutions for $\ell_{\rm u}^+$ and $\ell_{\rm w}^+$, which are assumed to possess a dilation group invariance and to take the following analytic form

$$\ell_{\rm u}^+ = \ell_{u0}^+(z^+)^{3/2}\left[1+\left(\frac{z^+}{z_{\rm sub}^+}\right)^4\right]^{1/4}, \tag{12}$$

$$\ell_{\rm w}^+ = \ell_{w0}^+(x^+)^{3/2}\left[1+\left(\frac{x^+}{x_{\rm sub}^+}\right)^4\right]^{1/4}, \tag{13}$$

where $z_{\rm sub}^+$ (and $x_{\rm sub}^+$) is the thickness of the viscous sublayer near the bottom (and side) wall. Note that Eqs. (12) and (13) present two asymptotic scalings—for $z^+ \ll z_{\rm sub}^+$ (and $x^+ \ll x_{\rm sub}^+$), $\ell_{\rm u}^+ \sim (z^+)^{3/2}$ (and $\ell_{\rm w}^+ \sim (x^+)^{3/2}$); and for $z^+ \gg z_{\rm sub}^+$ (and $x^+ \gg x_{\rm sub}^+$), $\ell_{\rm u}^+ \sim (z^+)^{5/2}$ (and $\ell_{\rm w}^+ \sim (x^+)^{5/2}$). The scaling exponent 3/2 is derived in Ref. [25], while the exponent 5/2 is due to a transition of $\partial\overline{u}/\partial z$ (and $\partial\overline{w}/\partial x$) from z^0 (and x^0) in the sublayer to z^{-1} (and x^{-1}) outside, which is specific to the RBC.

Figure 10a, b shows that MVPs can be accurately described by the two-layer stress length formula (12) and (13). The two-layer structure region extends up to $z^+ \approx 30$ for $Ra = 10^{10}$. At lower Ra, the flow at $z^+ \sim 20$ is bulk-dominated, having a relatively thin BL. The Ra-dependence of $z_{\rm sub}^+$ and ℓ_0 are shown in Fig. 10c, d, respectively. The fact is that ℓ_0^+ decreases monotonically as power functions—$\ell_{u0}^+ = 2.15Ra^{-0.125}$ for Eq. (12) and $\ell_{w0}^+ = 4.60Ra^{-0.235}$ for Eq. (13). The sublayer thickness $z_{\rm sub}^+ = 0.062Ra^{0.225}$ holds for two decades of Ra ($1 \times 10^8 \le Ra \le 1 \times 10^{10}$),

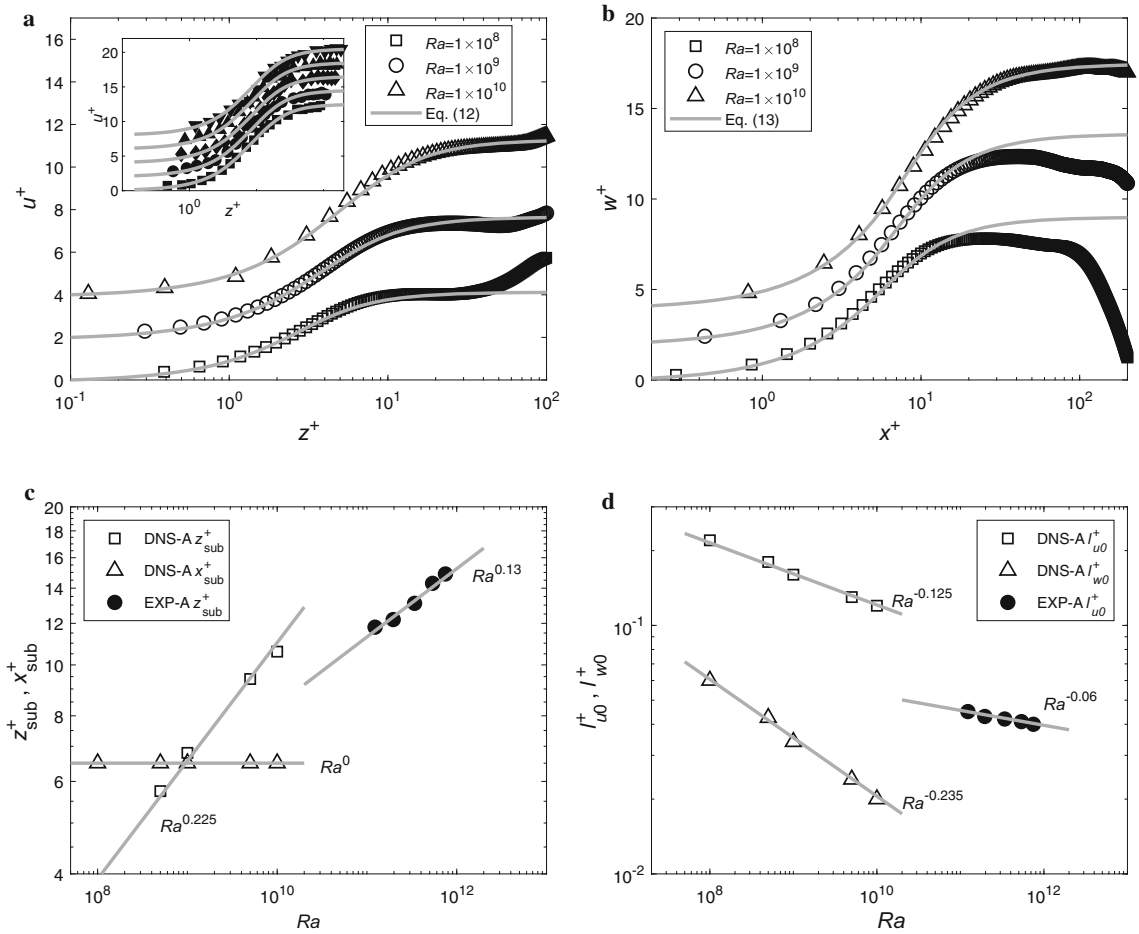

Fig. 10 **a** Comparison of the multilayer prediction for $U^+(z^+)$ [Eq. (12) plotted as a solid line] and the DNS-A data (symbols). The velocity profiles from Eq. (12) for the EXP-A data are shown in the inset, where ■, ●, ◆, ▲ and ▼ represent $Ra = 1.23 \times 10^{11}$, 1.96×10^{11}, 3.39×10^{11}, 5.58×10^{11} and 7.48×10^{11}, respectively. **b** Comparison of the multilayer prediction for $W^+(x^+)$ from Eq. (13) and the DNS-A data. **c** Parameters $z^+_{\rm sub}$ and $x^+_{\rm sub}$ as functions of Ra. **d** Parameters ℓ^+_{u0} and ℓ^+_{w0} as functions of Ra

whereas the convection in the cylindrical cell has a lower scaling, 0.13, as seen in Fig. 10c. This implies that the convection near the wall in a rectangular cell is stronger than that in a cylindrical cell, and inspires us to verify these scalings for different configurations over a wide range of Ra. For the sublayer on the sidewalls, the thickness is insensitive to Ra, i.e. $x^+_{\rm sub} \approx 6.50$.

3.3 Log-law of the thermal boundary layer

The existence of logarithmic temperature profiles in turbulent RBC has attracted much attention in recent years. The log thermal layer is usually attributed to plume emission near the conducting plates [16]. Here, we discuss the relation between the statistical behaviors of thermal structures and the logarithmic distribution of temperature.

According to the DNS, thermal dissipation in the horizontal direction can almost be ignored in the plume-ejecting region. Thus the temperature equation in the 2D form can be simplified as:

$$-\frac{\mathrm{d}\overline{\theta}}{\mathrm{d}(z/H)} + \frac{\overline{w\theta}H}{\kappa} = -\left.\frac{\mathrm{d}\overline{\theta}}{\mathrm{d}(z/H)}\right|_{z=0} \equiv Nu. \tag{14}$$

Denoting $S^*_\theta = -\mathrm{d}\overline{\theta}/(Nu\mathrm{d}(z/H)) = -\mathrm{d}\overline{\theta}/\mathrm{d}z^*$ and $W^*_\theta = \overline{w\theta}H/(\kappa Nu) = \overline{w\theta}^*$ gives the normalized mean temperature equation

$$S^*_\theta + W^*_\theta = 1, \tag{15}$$

with normalized vertical coordinate, $z^* = (z/H)Nu$. The thermal BL can be divided into three layers according to the mean momentum equation: (a) the near-wall region (the conduction layer), described by $S^*_\theta \simeq 1$; (b) the region far from the wall, dominated by $W^*_\theta \simeq 1$; (c) the layer between these two layers. Note that W^*_θ represents the convective heat flux by normal velocity fluctuations from the wall. The thermal balance in the form of the stress length similar to the

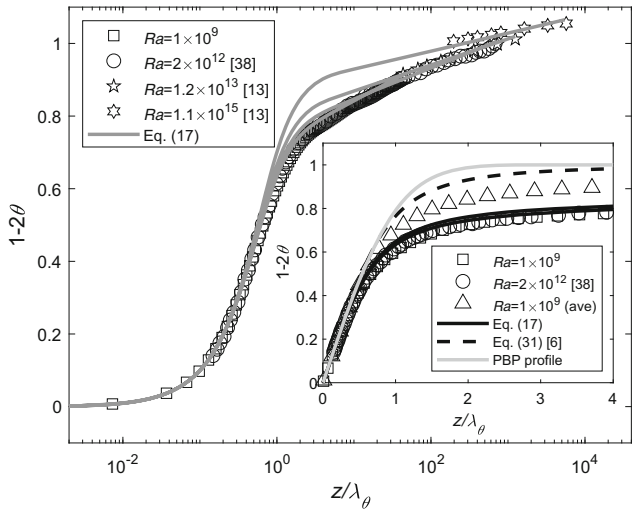

Fig. 11 MTP of three data sets: the present DNS, the DNS from Ref. [38], and the experiment from Ahlers et al. [13]. The solid lines indicate Eq. (17). The triangles are the MTP averaged along the horizontal (x) direction. The dashed line is the model of Eq. (31) in Ref. [6], and the gray curve is PBP profile

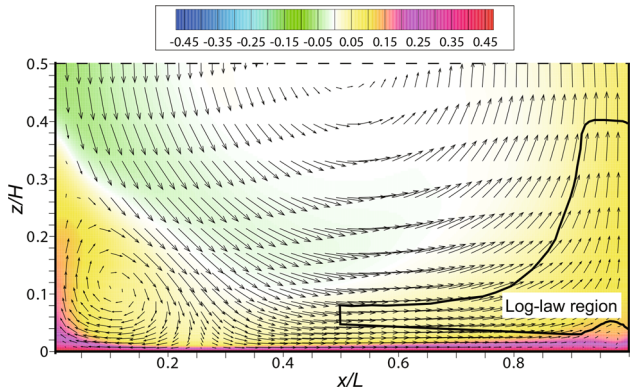

Fig. 12 (Color online) The log-law region of thermal BL described by Eq. (18) at $Ra = 1 \times 10^8$, marked by solid line. The pseudo-color denotes temperature. Cold color represents low temperature, and hot color high temperature. The arrows are the velocity vectors

momentum transport is obtained, and thus the temperature distribution is extracted.

We follow the SED theory [25] to quantify the MTP by postulating a similar (thermal) sublayer, buffer layer and log layer, with a temperature length ℓ_θ^* as the similarity variable, which plays a similar role as the stress length. Specifically, ℓ_θ^* displays a three-layer structure, i.e. $\ell_\theta^* \propto z^{*3/2}$ for $z^* < z_{\rm sub}^*$; $\ell_\theta^* \propto z^{*5/2}$ for $z_{\rm sub}^* < z^* < z_{\rm buf}^*$; and $\ell_\theta^* \propto z^*$ for $z^* > z_{\rm buf}^*$, where the superscript $*$ denotes the variable normalization by Nu/H. The first exponent 3/2 readily follows from a near-wall expansion, ignoring the fluctuation magnitude, where $S_\theta^* \to 1$ and $W_\theta^* \to z^{*3}$. The third layer has a linear scaling in z, corresponding to the log layer.

The buffer layer, similar to the role of the momentum buffer layer, is considered the transition from a laminar flow near the wall to a fully turbulent flow in the bulk. Inspecting the DNS, we obtain the scaling exponent 5/2 by invoking the integral scale of temperature fluctuation, $\ell_{\rm int}^* \equiv (W_\theta^*/S_\theta^*)^{3/4}/\epsilon_\theta^{1/4}$, proportional to $z^{*9/4}$ near the wall, and a dissipation-to-production ratio for temperature fluctuation, $\Theta_\theta \equiv \epsilon_\theta/(S_\theta^* W_\theta^*)$, proportional to z in the buffer layer. Since $\ell_\theta^* = \ell_{\rm int}^* \Theta_\theta^{1/4}$, it follows $\ell_\theta^* \propto z^{*5/2}$ in the buffer layer as a semi-empirical result. Finally, the SED theory postulates a generalized dilation symmetry that ℓ_θ^* displays a generalized Lie-group invariance characterizing the transition between the local scaling behaviors, yielding a composite solution of $\ell_\theta^*(z^*)$:

$$\ell_\theta^*(z^*) = \sqrt{W_\theta^*}/S_\theta^* = \ell_{\theta 0}^* z^{*3/2} \left[1 + \left(\frac{z^*}{z_{\rm sub}^*}\right)^4\right]^{\frac{1}{4}} \left[1 + \left(\frac{z^*}{z_{\rm buf}^*}\right)^4\right]^{-\frac{1.5}{4}}. \tag{16}$$

The stress length of temperature $\ell_\theta^*(z)$ is a three-layer function expressed as Eq. (16). Transition of the scaling of ℓ_θ^* from 3/2 to 5/2 occurs at $z_{\rm sub}^*$. The next transition of scaling from 5/2 to 1 is present at $z_{\rm buf}^*$.

Jointly solving Eqs. (15) and (16) yields an analytic function of the MTP as

$$1 - 2\overline{\theta}(z^*) = \int_0^{z^*} 2S_\theta \, {\rm d}z' = \int_0^{z^*} \frac{-1 + \sqrt{4\ell_\theta^{*2} + 1}}{\ell_\theta^{*2}} \, {\rm d}z'. \tag{17}$$

The first consequence of the solution is the logarithmic law of MTP. For $z^* \gg z_{\rm buf}^*$, $\ell_\theta^* \approx \kappa_\theta z^* \gg 1$, then $S_\theta^* \approx 1/(\kappa_\theta z^*)$, a logarithmic MTP follows

$$\overline{\theta} \approx -\frac{1}{\kappa_\theta} \ln z^* + B = -A \ln z^* + B, \tag{18}$$

$$A^{-1} = \kappa_\theta = \ell_{\theta 0}^* {z_{\rm buf}^*}^{3/2} {z_{\rm sub}^*}^{-1}. \tag{19}$$

Figure 11 shows the comparison between the analytic solutions at a fixed location from the side wall ($r = 0.0045$) for Ra covering six decades, from moderate ($Ra = 1 \times 10^9$) in DNS to the extremely high Ra experiments ($Ra = 1.1 \times 10^{15}$) [13]. The MTP in the plume-ejecting region clearly presents a log law covering at least one decade in z ($0.04 \leqslant z/H \leqslant 0.4$). Close inspection of Figs. 4 and 12 shows that the range of log-layer coincides with the intensive plume emission, indicating the relation between the two phenomena.

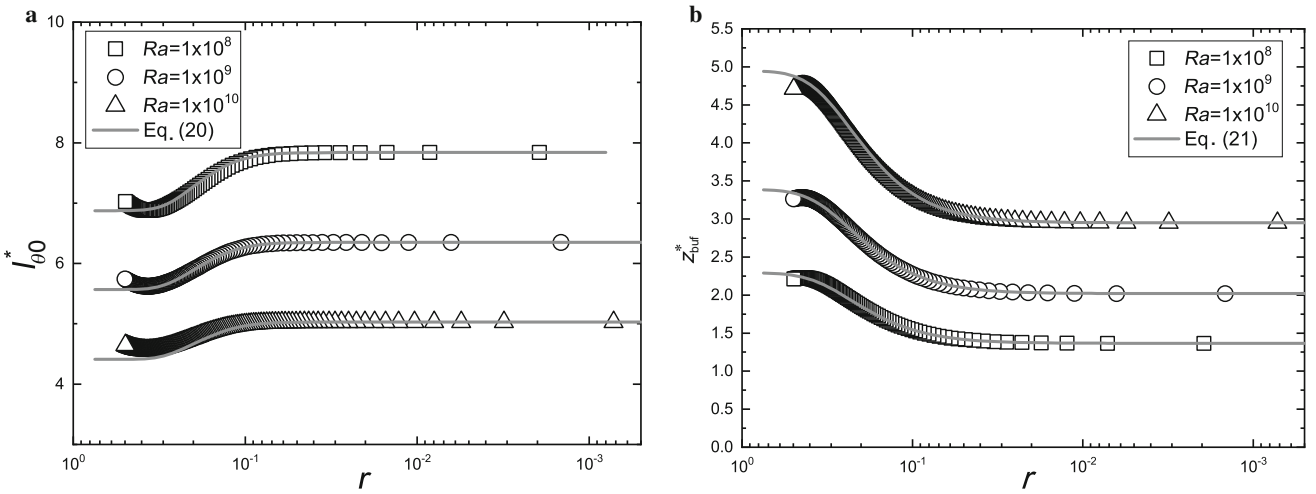

Fig. 13 **a** $\ell^*_{\theta 0}(r)$ and **b** $z^*_{\rm buf}(r)$ for $Ra = 1 \times 10^8$, 1×10^9 and 1×10^{10}, respectively. The solid lines are the multilayer function of Eq. (20). The solid lines are the multilayer function of Eq. (21)

We calculated the theoretical model, Eq. (31), for $Pr \gtrsim 1$ from Ref. [6], with parameter $c = 1$, see the inset of Fig. 11. The systematic deviations of the MTP ($Pr < 1$) from the equation and the PBP profile predictions are observed. The MTP in the plume-ejecting region no longer represents a typical turbulent BL. Thus, we calculated the MTP averaged along the horizontal (x) direction, which represents the characteristics of BL in the wind-shearing region [6]. The inset of Fig. 11 shows that the space-averaged MTP is markedly higher than local MTP in the plume-ejecting region, and much closer to the BL equation. Though MTP in the wind-shearing region with small Pr has a trend similar to the case with large Pr, neither the present MTP nor that from Stevens et al. [38] ($Pr = 0.7$) can be described by the equation for $Pr \gtrsim 1$. However, an improved thermal BL equation is capable of describing the flow with a low Prandtl number down to 0.01 [50].

Three parameters, $\ell^*_{\theta 0}$, $z^*_{\rm sub}$ and $z^*_{\rm buf}$, are determined by measuring $l^*_\theta(z^*)$ from DNS. Since thermal dissipation dominates the BL near the side wall ($r < 0.1$ for DNS-A), the heat transport from convection is neglected in this region. Measurement of $z^*_{\rm sub}$ indicates that $z^*_{\rm sub} \simeq 0.375$. Two other parameters, $\ell^*_{\theta 0}$ and $z^*_{\rm buf}$, are found to be r-dependent—$\ell^*_{\theta 0}$ and $z^*_{\rm buf}$ are expressed in form of two-layer structures, expressed as the functions of $r = (1 - x/L)$:

$$\ell^*_{\theta 0} = \ell^*_{\theta 0,a}\left[1+\left(\frac{r}{r_b}\right)^4\right]^{-\frac{0.15}{4}}\left[1+\left(\frac{r}{r_c}\right)^4\right]^{\frac{0.15}{4}}, \quad (20)$$

$$z^*_{\rm buf} = z^*_{{\rm buf},a}\left[1+\left(\frac{r}{r_b}\right)^2\right]^{\frac{0.5}{2}}\left[1+\left(\frac{r}{r_c}\right)^4\right]^{-\frac{0.5}{4}}. \quad (21)$$

Near the side wall ($r \ll r_b$), $\ell^*_{\theta 0}$ and $z^*_{\rm buf}$ are constants denoted as $\ell^*_{\theta 0,a}$ and $z^*_{{\rm buf},a}$. The coefficient, $\ell^*_{\theta 0,a}$, may be associated with the size of thermal plumes, which decreases for increasing Ra, to be determined in the following section. In the wind-shearing region ($r \gg r_b$), we have a scaling $\ell^*_{\theta 0} \sim r^{-0.15}$, which decreases with increasing r, see Fig. 13a. On the other hand, the thickness of buffer layer $z^*_{\rm buf}$, as shown in Fig. 13b, increases in r, indicating that the thermal BL becomes thinner moving downstream with the wind (for increasing x or decreasing r).

After comparing the data sets, we find that $r_{\rm b} \simeq 0.125$ and $r_{\rm c} \simeq 0.35$ for the slim box (for DNS – A), but $r_b \simeq 0.0075$ and $r_c \simeq 0.35$ for the cylindrical cell (DNS – B)—they are likely independent of Ra. On the other hand, the coefficients $\ell^*_{\theta 0,a}$ and $z^*_{{\rm buf}0,a}$ depend on Ra, see Fig. 14. Specifically, $z^*_{{\rm buf}0,a} \approx 0.082 Ra^{0.155}$ for the slim-box simulations (DNS – A), but $0.046 Ra^{0.155}$ for the cylindrical cell (DNS – B). The same scaling of 0.155 for Ra indicates similar behavior of the heat transport near the side walls. Moreover, $\ell^*_{\theta 0,a} \simeq 63.0 Ra^{-0.11}$ for the slim box (DNS – A), but $46.0 Ra^{-0.11}$ for the cylindrical cell, also with the same scaling of -0.11 (see the inset of Fig. 14). Since $z^*_{\rm sub} \simeq 0.375$ is independent of Ra and geometry, matching condition for $A^{-1} \simeq \ell^*_{\theta 0} {z^*_{\rm buf}}^{3/2} {z^*_{\rm sub}}^{-1}$ yields a scaling for the coefficient of the log-law slope, $A \sim Ra^{0.1225}$, near the side wall, in good agreement with the experimental result of Ahlers et al. [12]: $A \sim Ra^{0.123}$.

The coefficient in the log-law $A = 1/\kappa_\theta$ as the function of x was first discussed in Ref. [26], suggesting an analytic form, $|A| = |A_1|/\sqrt{[4x(1-x)]}$ for the cylindrical cell. Note that $A(x)$ holds a $-1/2$-scaling (i.e. $A \sim A_0/\sqrt{x}$ for $x \to 0$). More recently, Ahlers et al. [13] claimed that the scaling was -0.65, due to an elliptical path (rather than a circular path) of the LSC. In the present study, for $z^* \gg z^*_{\rm buf}$, Eq. (16) can be rewritten as $\ell^*_\theta = [\ell^*_{\theta 0} {z^*_{\rm buf}}^{3/2} {z^*_{\rm sub}}^{-1}]z^*$, i.e. $\kappa_\theta = A^{-1} \simeq \ell^*_{\theta 0} {z^*_{\rm buf}}^{3/2} {z^*_{\rm sub}}^{-1}$. Based on the aforementioned analysis on ℓ^*_θ and $z^*_{\rm buf}$ (i.e. $\ell^*_{\theta 0} \sim r^{-0.15}$, $z^*_{\rm buf} \sim r^{0.5}$, and

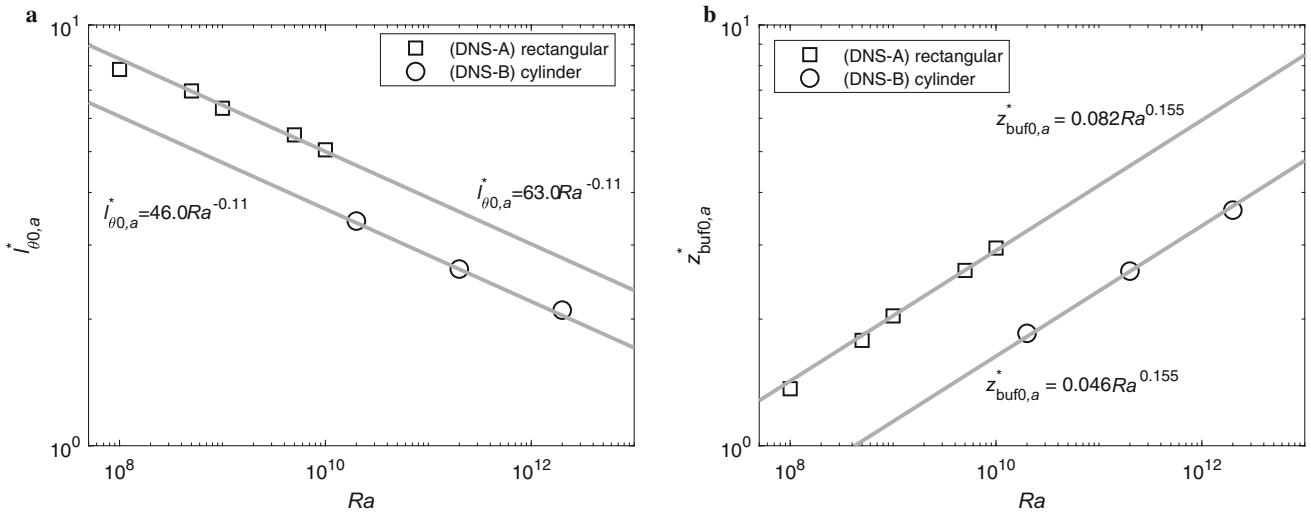

Fig. 14 Ra-dependence of **a** $\ell^*_{\theta 0,a}$ and **b** $z^*_{\mathrm{buf}0,a}$

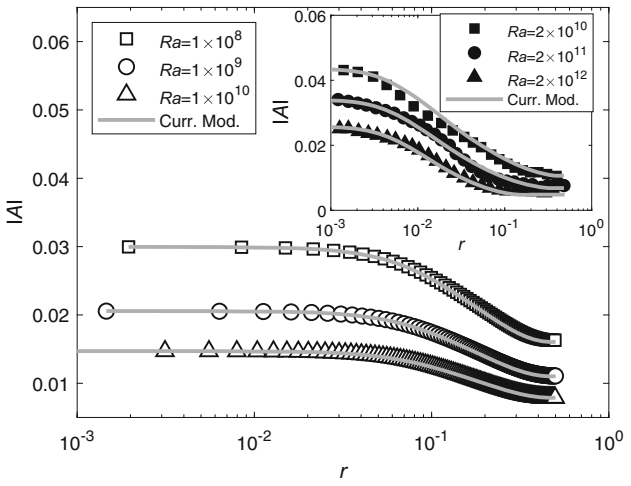

Fig. 15 Parameter A of the log-law function varies with the longitudinal coordinate x for different Ras in DNS-A. The inset is the result of DNS-B. The solid lines represent $A \simeq z^*_{\mathrm{sub}} / \left(\ell^*_{\theta 0} {z^*_{\mathrm{buf}}}^{3/2}\right)$

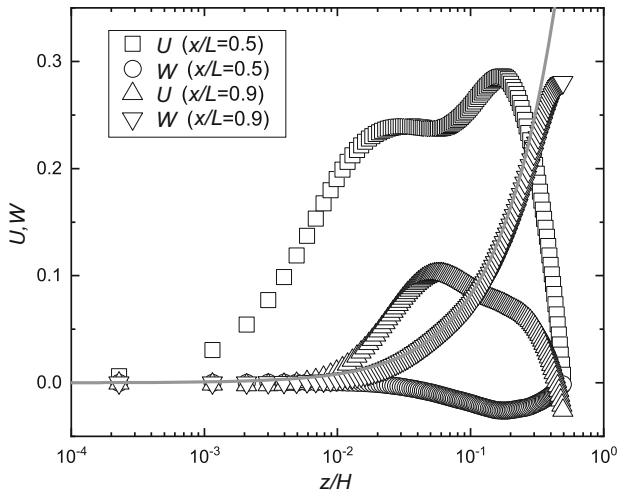

Fig. 16 Horizontal $U(z)$ and vertical velocity $W(z)$ profiles in the plume-ejecting region at $x/L = 0.9$ and the wind-shearing region at $x/L = 0.5$ for the case of $Ra = 1 \times 10^8$. The solid line is the fitting of $W/U_0 = 0.7(z/H)$

z^*_{sub} = const.), we have $A \sim r^{-0.60}$, in agreement with the recent result of Grossmann and Lohse [26]. Figure 15 presents the comparison between our predicted coefficient $A(r)$ from DNS at different Ras, which is superior to the fitting function of Ref. [26]; the latter is only valid in a restricted domain ($0.02 < r < 0.2$ for $Ra = 2 \times 10^{12}$ from Ref. [13]). Thus, the current model gives a unified description of A valid over the wider flow domain, from the side wall ($r = 0$) to the wind-shearing region.

To investigate the dynamics in the log layer, we calculated the profiles of the horizontal and vertical velocity in the plume-ejecting and wind-shearing regions, as presented in Fig. 16. No logarithmic region for $U(z)$ is found in the plume-ejecting region. It is reasonable to believe that the log layer of temperature has an origin free from the log viscous BL; in other words, the Reynolds analogy does not hold here. It is interesting to make a comparison between velocities in the wind-shearing region ($0.25 \lesssim x/L \lesssim 0.75$) and those in the plume-ejecting region ($x/L \gtrsim 0.75$). The flow is governed by strong APG due to the confinement of the sidewalls, and the momentum is changed from a horizontal to an upward direction in the plume-ejecting region. The overlapping of the plume-ejecting region with the log thermal BL indicates that vertical momentum plays the main role in establishing the log law of temperature. In addition, the vertical velocity is found to be approximately proportional to the wall distance, $W/U_0 = 0.7(z/H)$ at $0 \leqslant z/H \leqslant 0.4$ in the plume-ejecting region, as shown in Fig. 16.

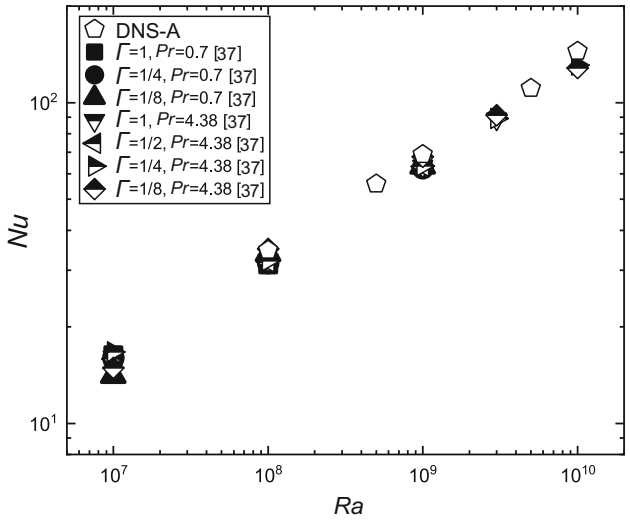

Fig. 17 Compensated Nu as a function of Ra

3.4 Rayleigh number effect on heat transport

One of the main issues in the study of RBC is determining the dimensionless heat transfer coefficient, the Nusselt number Nu. The heat flux can be calculated by $Nu(z) = \langle w\theta/\kappa - \partial\theta/\partial z\rangle_{x,y,t}$, where $\langle\cdot\rangle_{x,y,t}$ represents averaging over the horizontal plane and sufficient length of time. A comparison between Nu of the present simulation with previous data is presented in Fig. 17. Note that the DNS by Kaczorowski et al. [37] examined various aspect ratios (varying from $\Gamma = 1/8$ to $\Gamma = 1$) and Prandtl numbers ($Pr = 0.7$ and 4.3). The slim-box simulations agree with other data at the same Pr (i.e. $Pr = 0.7$), but our Nu is slightly larger than that of Ref. [37]. This is consistent with the fact that the slim box enhances the LSC and thus a more intensive heat transport.

We now examine the contribution of each flow region to total heat transport by calculating $Nu_{\rm loc}(x,z) = \langle w\theta/\kappa - \nabla\theta\rangle_{y,t}$, where $\langle\cdot\rangle_{y,t}$ denotes the averaging over the depth direction and sufficient length of time. Figure 18a shows $Nu_{\rm loc}(x,0)/Nu$ at the bottom plate (i.e. $z = 0$), which is dominated by thermal diffusion $Nu_{\rm loc}(x,0) \approx -\nabla\theta(x,0)$. Note that the maximum heat flux appears at $x = 0.25$, where the thickness of the thermal BL is the thinnest, as shown in Fig. 18a, corresponding to where the cold plumes impinge on the heating plate. The total heat flux in the range of $0 \leqslant x \leqslant 0.25$ corresponds to that by the corner roll.

In the center region ($0.25 \lesssim x/L \lesssim 0.75$), our computation shows a linearly decreasing heat flux with increasing x, corresponding to an increase in the thermal BL thickness, consistent with other data [10,48]. However, this decreasing trend is weakened at higher Ra, and the flow becomes more homogeneous in the horizontal direction. Figure 18b shows the local heat flux $Nu_{\rm loc}$ at half the height of the box ($z/H = 0.5$). For $Ra = 1 \times 10^8$, $Nu_{\rm loc}$ is more symmetrical with respect to $z/H = 0.5$ than $z = 0$, which is due to the heat convection by the LSC. The three flow regions, i.e. plume-impacting ($0 \leqslant x/L \leqslant 0.25$), wind-shearing ($0.25 \leqslant x/L \leqslant 0.75$) and plume-ejecting ($0.75 \leqslant x/L \leqslant 1$) regions, are rather distinct, as shown in Fig. 18a, which is also clearly observed for $Ra = 1 \times 10^9$. Convective heat transfer is predominant in the heat flux near the centerline $z/H = 0.5$. We find that there is a symmetry breaking in the vertical velocity $W(x)$ near the centerline, the maximum magnitude

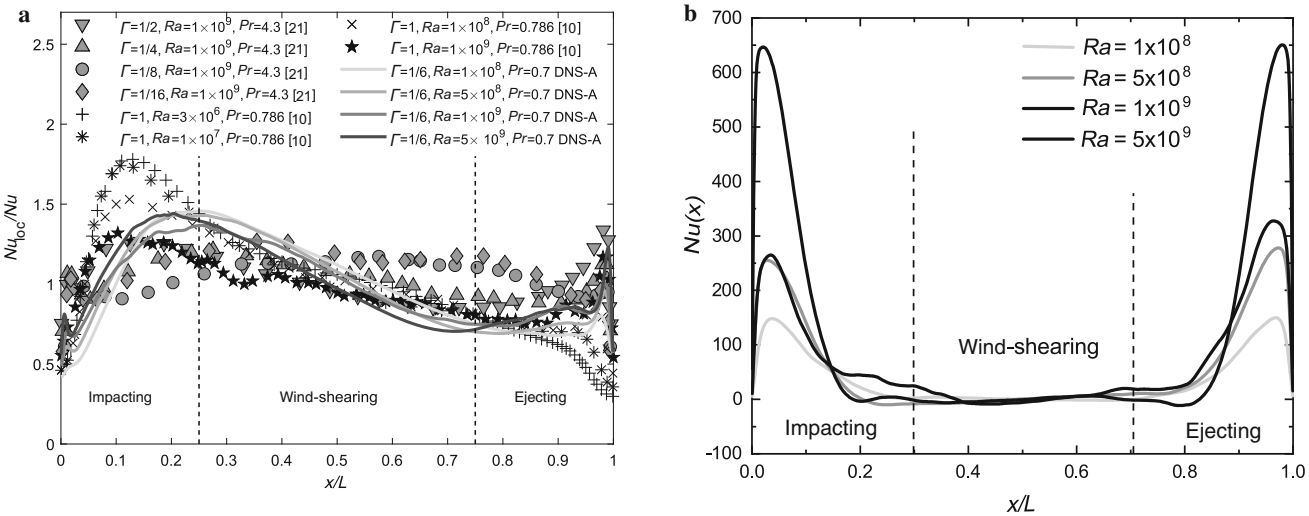

Fig. 18 **a** Local heat flux $Nu_{\rm loc}/Nu$ (normalized with global Nusselt number, Nu) at the bottom plate (i.e. $z = 0$) varying with x [10,21]. **b** $Nu_{\rm loc}$ at the half height of the convection box ($z/H = 0.5$) varying with x

of W is 0.271 on the right side, greater than -0.243 on the left side, leading to the higher local heat flux at $x = 0$ side.

4 Concluding remarks

We performed the 3D DNS of RBC at $Pr = 0.7$ and $Ra = 1 \times 10^8 \sim 1 \times 10^{10}$ for a slim box (the ratio of length, depth and height is 1:1/6:1), with periodic boundary condition in the depth (y) direction. Two facts for the slim-box RBC are found: (a) the LSC is steadily confined parallel to the $x-z$ plane, and (b) a higher heat flux and stronger LSC is observed, in contrast to the cases in a confined cell, as a result of the absence of front/back walls. Three flow regions (i.e. plume-impacting, wind-shearing, and plume-ejecting) are clearly revealed in the time-averaged distribution of velocity and temperature.

The non-Blasius velocity profiles under the influence of a strong adverse pressure gradient can be described by the multilayer stress-length function, following the symmetry-based theory of canonical wall turbulence [25]. The MTPs can be satisfactorily described by a multilayer structure of a thermal dissipation stress-length function, which yields an analytic description of the log-law coefficient A for a range of x and Ra. Certain parameters, namely ℓ_{u0}, ℓ_{w0}, $\ell_{\theta 0}$, and z_{buf}, in the stress-length functions for viscous and thermal BLs are found to be influenced by Ra, Pr, and even the geometry of the convection cell. Parameterization of the multilayer functions for various configurations can be fulfilled by investigating additional experiments and numerical simulations. Moreover, with knowledge of the symmetry in each layer, these stress-length functions can be applied to interpret and predict the convection flow at extreme conditions, for example, high Ra or high/low Pr.

Local heat transport is analyzed and discussed. The Nusselt number scaling and local heat flux of the present simulations are consistent with previous experiments [21] and numerical simulations [37] in the confined rectangular cell. Thus, we conclude that the present slim-box RBC is an ideal system for studying in-box kinetic and thermal structures, and space-time correlations [51], in confined turbulent convection.

Acknowledgements The Project was supported by the National Natural Science Foundation of China (Grants 11452002, 11521091, and 11372362) and MOST (China) 973 Project (Grant 2009CB724100).

References

1. Xia, K.Q.: Current trends and future directions in turbulent thermal convection. Theor. Appl. Mech. Lett. **3**, 052001 (2013)
2. Liu, C., Tang, S., Shen, L., et al.: Characteristics of turbulence transport for momentum and heat in particle-laden turbulent vertical channel flows. Acta Mech. Sinica **33**, 833–845 (2017)
3. Gao, Z.Y., Luo, J.H., Bao, Y.: Numerical study of heat-transfer in two- and quasi-two-dimensional Rayleigh–Bénard convection. Chin. Phys. B **27**, 104702 (2018)
4. Chen, J., Bao, Y., Yin, Z.X., et al.: Theoretical and numerical study of enhanced heat transfer in partitioned thermal convection. Int. J. Heat Mass Transf. **115**, 556–569 (2017)
5. Bao, Y., Chen, J., Liu, B.F., et al.: Enhanced heat transport in partitioned thermal convection. J. Fluid Mech. **784**, R5 (2015)
6. Shishkina, O., Horn, S., Wagner, S., et al.: Thermal boundary layer equation for turbulent Rayleigh–Bénard convection. Phys. Rev. Lett. **114**, 114302 (2015)
7. Wang, Y., He, X., Tong, P.: Boundary layer fluctuations and their effects on mean and variance temperature profiles in turbulent Rayleigh–Bénard convection. Phys. Rev. Fluids **1**, 082301 (2016)
8. Zhou, Q., Stevens, R.J.A.M., Sugiyama, K., et al.: Prandtl–Blasius temperature and velocity boundary-layer profiles in turbulent Rayleigh–Bénard convection. J. Fluid Mech. **664**, 297312 (2010)
9. van der Poel, E.P., Stevens, R.J., Lohse, D.: Comparison between two-and three-dimensional Rayleigh–Bénard convection. J. Fluid Mech. **736**, 177–194 (2013)
10. Wagner, S., Shishkina, O., Wagner, C.: Boundary layers and wind in cylindrical Rayleigh–Bénard cells. J. Fluid Mech. **697**, 336–366 (2012)
11. Shi, N., Emran, M.S., Schumacher, J.: Boundary layer structure in turbulent Rayleigh–Bénard convection. J. Fluid Mech. **706**, 5–33 (2012)
12. Ahlers, G., Bodenschatz, E., He, X.: Logarithmic temperature profiles of turbulent convection in the classical and ultimate state for a Prandtl number of 0.8. J. Fluid Mech. **758**, 436467 (2014)
13. Ahlers, G., Bodenschatz, E., Funfschilling, D., et al.: Logarithmic temperature profiles in turbulent Rayleigh–Bénard convection. Phys. Rev. Lett. **109**, 114501 (2012)
14. Wei, P., Ahlers, G.: Logarithmic temperature profiles in the bulk of turbulent Rayleigh–Bénard convection for a Prandtl number of 12.3. J. Fluid Mech. **758**, 809830 (2014)
15. Shishkina, O., Wagner, C.: Local heat fluxes in turbulent Rayleigh–Bénard convection. Phys. Fluids **19**, 085107 (2007)
16. van der Poel, E.P., Ostilla-Mónico, R., Verzicco, R., et al.: Logarithmic mean temperature profiles and their connection to plume emissions in turbulent Rayleigh–Bénard convectionvan. Phys. Rev. Lett. **115**, 154501 (2015)
17. Huang, S.D., Wang, F., Xi, H.D., et al.: Comparitive experimental study of fixed temperature and fixed heat flux boundary condidtions in turbulent thermal convection. Phys. Rev. Lett. **115**, 154502 (2015)
18. Xi, H.D., Zhang, Y.B., Hao, J.T., et al.: High-order flow modes in turbulent Rayleigh–Bénard convection. J. Fluid Mech. **805**, 31–51 (2016)
19. Vasiliev, A., Sukhanovskii, A., Frick, P., et al.: High rayleigh number convection in a cubic cell with adiabatic sidewalls. Int. J. Heat Mass Transf. **102**, 201–212 (2016)
20. Podvin, B., Sergent, A.: Proper orthogonal decomposition investigation of turbulent Rayleigh–Bénard convection in a rectangular cavity. Phys. Fluids **24**, 105106 (2012)
21. Huang, S.D., Kaczorowski, M., Ni, R., et al.: Confinement-induced heat-transport enhancement in turbulent thermal convection. Phys. Rev. Lett. **111**, 104501 (2013)
22. Zhou, W.F., Chen, J.: Similarity model for corner roll in turbulent Rayleigh–Bénard convection. Phys. Fluids **30**, 111705 (2018)
23. van der Poel, E.P., Verzicco, R., Grossmann, S., et al.: Plume emission statistics in turbulent Rayleigh–Bénard convection. J. Fluid Mech. **772**, 5–15 (2015)
24. Chong, K.L., Xia, K.Q.: Exploring the severely confined regime in Rayleigh–Bénard convection. J. Fluid Mech. **805**, R4 (2016)

25. She, Z.S., Chen, X., Hussain, F.: Quantifying wall turbulence via a symmetry approach: a lie group theory. J. Fluid Mech. **827**, 322–356 (2017)
26. Grossmann, S., Lohse, D.: Logarithmic temperature profiles in the ultimate regime of thermal convection. Phys. Fluids **24**, 125103 (2012)
27. Verzicco, R., Camussi, R.: Numerical experiments on strongly turbulent thermal convection in a slender cylindrical cell. J. Fluid Mech. **477**, 19–49 (2003)
28. Verzicco, R., Orlandi, P.: A finite-difference scheme for three-dimensional incompressible flows in cylindrical coordinates. J. Comput. Phys. **123**, 402–414 (1996)
29. Kim, J., Moin, P.: Application of a fractional-step method to incompressible navier-stokes equations. J. Comput. Phys. **59**, 308–323 (1985)
30. Rai, M.M., Moin, P.: Direct simulations of turbulent flow using finite-difference schemes. J. Comput. Phys. **96**, 15–53 (1991)
31. Sun, X.H.: Application and accuracy of the parallel diagonal dominant algorithm. Parallel Comput. **21**, 1241–1267 (1995)
32. Shishkina, O., Stevens, R.J., Grossmann, S., et al.: Boundary layer structure in turbulent thermal convection and its consequences for the required numerical resolution. New J Phys. **12**, 075022 (2010)
33. Scheel, J.D., Emran, M.S., Schumacher, J.: Resolving the fine-scale structure in turbulent Rayleigh–Bénard convection. New J. Phys. **15**, 113063 (2013)
34. Shraiman, B.I., Siggia, E.D.: Heat transport in high-Rayleigh-number convection. Phys. Rev. A **42**, 3650 (1990)
35. Sun, C., Cheung, Y.H., Xia, K.Q.: Experimental studies of the viscous boundary layer properties in turbulent Rayleigh–Bénard convection. J. Fluid Mech. **605**, 79–113 (2008)
36. Wei, P., Xia, K.Q.: Viscous boundary layer properties in turbulent thermal convection in a cylindrical cell: the effect of cell tilting. J. Fluid Mech. **720**, 140–168 (2013)
37. Kaczorowski, M., Chong, K.L., Xia, K.Q.: Turbulent flow in the bulk of Rayleigh–Bénard convection: aspect-ratio dependence of the small-scale properties. J. Fluid Mech. **747**, 73–102 (2014)
38. Stevens, R.J.A.M., Lohse, D., Verzicco, R.: Prandtl and Rayleigh number dependence of heat transport in high rayleigh number thermal convection. J. Fluid Mech. **688**, 31–43 (2011)
39. du Puits, R., Resagk, C., Thess, A.: Mean velocity profile in confined turbulent convection. Phys. Rev. Lett. **99**, 234504 (2007)
40. Krishnamurti, R., Howard, L.N.: Large-scale flow generation in turbulent convection. In: Proceedings of the National Academy of Sciences, vol 78. National Academy of Sciences (1981)
41. Qiu, X.L., Xia, K.Q.: Spatial structure of the viscous boundary layer in turbulent convection. Phys. Rev. E **58**, 5816–5820 (1998)
42. Niemela, J.J., Skrbek, L., Sreenivasan, K.R., et al.: The wind in confined thermal convection. J. Fluid Mech. **449**, 169–178 (2001)
43. Benzi, R., Verzicco, R.: Numerical simulations of flow reversal in Rayleigh–Bénard convection. Europhys. Lett. **81**, 64008 (2008)
44. Sugiyama, K., Calzavarini, E., Grossmann, S., et al.: Flow organization in two-dimensional non-Oberbeck–Boussinesq Rayleigh–Bénard convection in water. J. Fluid Mech. **637**, 105–135 (2009)
45. Zhou, Q., Sugiyama, K., Stevens, R.J.A.M., et al.: Horizontal structures of velocity and temperature boundary layers in two-dimensional numerical turbulent Rayleigh–Bénard convection. Phys. Fluids **23**, 125104 (2011)
46. van Reeuwijk, M., Jonker, H.J.J., Hanjalić, K.: Wind and boundary layers in Rayleigh–Bénard convection. I. Analysis and modeling. Phys. Rev. E **77**, 036312 (2008)
47. van Reeuwijk, M., Jonker, H.J.J., Hanjalić, K.: Wind and boundary layers in Rayleigh–Bénard convection. II. Boundary layer character and scaling. Phys. Rev. E **77**, 036311 (2008)
48. Xia, K.Q., Sun, C., Zhou, S.Q.: Particle image velocimetry measurement of the velocity field in turbulent thermal convection. Phys. Rev. E **68**, 066303 (2003)
49. Qiu, X.L., Tong, P.: Large-scale velocity structures in turbulent thermal convection. Phys. Rev. E **64**, 036304 (2001)
50. Shishkina, O., Horn, S., Emran, M.S., et al.: Mean temperature profiles in turbulent thermal convection. Phys. Rev. Fluids **2**, 113502 (2017)
51. He, X., Tong, P.: Space-time correlations in turbulent Rayleigh–Bénard convection. Acta Mech. Sinica **30**, 457–467 (2014)